Journal of Materials Chemistry C

ROYAL SOCIETY OF CHEMISTRY

PAPER

View Article Online
View Journal | View Issue

Cite this: J. Mater. Chem. C, 2022, 10, 16723

$Sc_{1-x}Er_xAlO_3$ perovskites: high-pressure synthesis, photoluminescence properties, and *in vitro* bioimaging†

Debendra Prasad Panda,[a] Akash Kumar Singh,[b] Tapas K. Kundu[b] and A. Sundaresan *[a]

Received 27th September 2022,
Accepted 28th October 2022

DOI: 10.1039/d2tc04092a

rsc.li/materials-c

Optical imaging carries cellular-level information and is a new paradigm as an imaging modality. Importantly, rare-earth ion-doped metal oxide imaging agents have certain advantages like sharp emission lines, long luminescence lifetimes, low cytotoxicity, and enhanced photostability over organic dyes and quantum dots and are highly desirable. In this context, we have prepared $Sc_{1-x}Er_xAlO_3$ perovskite phosphors using the high-pressure synthetic method, which crystallize in an orthorhombic structure (*Pbnm* space group). Under UV light excitation, they exhibit green luminescence with sharp emission lines and PL lifetimes in the order of microseconds. The temperature-dependent measurement suggests the high thermal photostability of the perovskite compound, which altogether indicates its potential for optical imaging. The 2% Er^{3+} substituted compound incubated in HEK293 and SH-SY5Y cells exhibits very low cytotoxicity. Using a two-photon microscope, the biocompatibility of this compound in HEK293 cells was imaged, stipulating its potential biomedical application.

1. Introduction

Perovskites are a class of compounds which have been investigated meticulously in recent decades since the discovery of ferroelectricity in $BaTiO_3$. They have revolutionized the field of materials science owing to their potential to exhibit multifunctional properties such as magnetism, ferroelectricity, multiferroicity, superconductivity, thermoelectricity, catalysis, luminescence properties and so on.[1–8] Recently, halide perovskites also exhibited fascinating luminescence properties such as while light emission and enhanced lasing performances.[9–12] Multifarious synthetic approaches such as solid-state synthesis, sol–gel, hydrothermal methods, *etc.* have been employed to design new metal oxide perovskites. However, some compounds cannot be synthesized using the aforementioned techniques. High-pressure synthesis, a recently added wing in solid-state chemistry, is beneficial for stabilizing some metastable compounds under ambient conditions.[13,14] In recent times, high-pressure synthesized perovskites have been studied for their different fascinating properties; however, their photoluminescence properties are seldom explored. Mostly, metal oxide perovskites are non-luminescent, but can act as a host for incorporating rare-earth ions, which can induce emissive properties.[15,16] Hence, designing a host lattice is important with high structural rigidity, which can lead to an efficient phosphor for rare-earth ion activation.[17]

Rare-earth ion incorporation in an optically silent lattice can successfully activate photoluminescence properties and can be helpful in designing new luminescent materials.[16,18,19] Since they involve parity forbidden f–f transitions, noncentrosymmetric site occupation is important to display electric dipole moment-induced intense emission.[15,20] These phosphors exhibit sharp emission spectra, large Stokes shifts, long lifetime of photoexcited electrons, and high photostability.[21,22] Among rare-earth ion-activated phosphors, Er^{3+} doped compounds have been rigorously investigated for their potential to display tunable emission. Under UV light excitation, Er^{3+}-activated compounds exhibit green emission as a result of down-conversion.[23,24] On the other hand, it shows red emission with a sensitizer like Yb^{3+} due to the upconversion process under NIR excitation.[25,26] Further, they are promising candidates for light-emitting diodes, optical thermometry, and cell imaging applications, which make them more interesting.[27–30]

Nowadays, imaging modalities like magnetic resonance imaging (MRI), X-ray computed tomography (CT), thermal imaging, ultrasound, optical imaging, *etc.* have emerged as indispensable techniques for biomedical applications.[31–34] Amidst these

[a] School of Advanced Materials, and Chemistry and Physics of Materials Unit, Jawaharlal Nehru Centre for Advanced Scientific Research, Jakkur, Bangalore 560064, India. E-mail: sundaresan@jncasr.ac.in
[b] Transcription and Disease Laboratory, Molecular Biology and Genetics Unit, Jawaharlal Nehru Centre for Advanced Scientific Research, Jakkur, Bangalore 560064, India

† Electronic supplementary information (ESI) available. See DOI: https://doi.org/10.1039/d2tc04092a

noninvasive imaging modalities, optical imaging has been proved to be a prime technique owing to its high spatial resolution and sensitivity.[35] Optical imaging carries cellular level information which helps to target specific cells for molecular diagnostics. Mostly, fluorescent proteins, organic dyes, and quantum dots are used as probes for optical imaging. However, the photobleaching and short PL lifetime restrict the use of fluorescent proteins and organic dyes.[36] Quantum dots also suffer from low stability, photo-blinking and toxicity, and are detrimental as a bio-probe.[37,38] Hence, rare-earth activated metal oxides are the recent sensation which can exhibit sharp emission spectra, long luminescence lifetimes, enhanced stability in cell medium, and low cytotoxicity.[38–40] In addition, the bulk compounds are more beneficial over nanoparticles due to high luminescence intensity.[41]

Motivated by the above results, we have attempted to employ a high-pressure synthesized Er^{3+}-activated phosphor for cell imaging. The $Sc_{1-x}Er_xAlO_3$ perovskites crystallize in the orthorhombic *Pbnm* space group, where Er^{3+} ions occupy a polar site symmetry *m*. Upon UV light excitation, they exhibit green luminescence with the lifetime of photoexcited electrons in the order of microseconds. Investigation of temperature-dependent emission spectra stipulates high thermal photostability useful for optoelectronic applications. We also analyzed the cell viability of HEK293 and SH-SY5Y cells in the presence of this compound. The low cytotoxicity motivated us to perform *in vitro* cell adhesion experiments, which confirm that these perovskite particles can be used as a probe for *in vivo* bioimaging.

2. Experimental

2.1. Synthesis

Polycrystalline samples of $Sc_{1-x}Er_xAlO_3$ (x = 0.01, 0.02, 0.03, 0.04) were prepared using the high-pressure synthesis method. First, stoichiometric amounts of Sc_2O_3, Al_2O_3, and Er_2O_3 were ground and packed in a gold capsule. Prior to that, Er_2O_3 was preheated at 900 °C for 12 h. The gold capsule was placed in a graphite sleeve containing a mixture of NaCl and ZrO_2. Later, a pyrophyllite stone was used as a pressure mediating medium and the assembly is shown in Scheme 1. A pressure of 4.5 GPa was applied and heated to 1000 °C for 1 h, followed by quenching the sample to room temperature.

2.2. Characterization

Room temperature powder X-ray diffraction measurement was carried out for structural analysis of the compounds using a PANalytical Empyrean diffractometer with Cu $K\alpha_1$ radiation (λ = 1.54059 Å). Field emission scanning electron microscopy (FESEM) and energy dispersive X-ray spectroscopy (EDS) measurements were performed using a Thermo Fisher Apreo 2 S instrument. Heat capacity was measured using a Physical Property Measurement System (PPMS; Quantum Design, USA).

2.3. Optical property measurement

A PerkinElmer Lambda 750 spectrometer was used to record the UV-VIS diffuse reflectance spectra of the samples. The background was corrected using a $BaSO_4$ disk. The steady-state excitation and emission spectra are recorded using an Edinburg FLS1000 spectrometer fitted with a 450 W xenon lamp. The time-resolved measurements were carried out using a microsecond lamp in the same instrument. For temperature-dependent spectra, a helium cryostat was used.

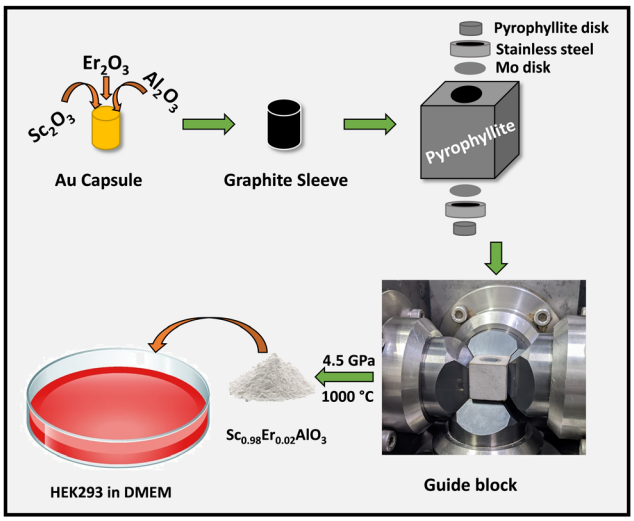

Scheme 1 High-pressure synthesis and cell adhesion of the $Sc_{1-x}Er_xAlO_3$ perovskite compound.

2.4. Cell culture and MTT cell viability assays

For *in vitro* cell cytotoxicity, the MTT assay was performed on SH-SY5Y neuroblastoma cells as well as HEK293 Human Embryo Kidney cells. Cells were grown in complete media (DMEM supplemented with 10% FBS) in a 25 ml tissue culture flask and maintained at 37 °C with a 5% CO_2 atmosphere in a humidified chamber. For the cell viability assay, cells were trypsinized at 85–90% confluency, and 10^4 cells were seeded in 96-well plates for the MTT assay. The cells were allowed to grow for 24 hours and then treated with different doses of the compound for 24 hours. The growth medium was removed after 24 hours, and cells were washed twice with 1× PBS. Then tetrazolium dye MTT (prepared in growth media) was added. Cell viability was calculated by the MTT assay as instructed in the manufacturer's protocol. The viability of untreated cells was kept at 100% and comparatively the cell viability of all the groups treated with varying concentrations of the compound was calculated. For each group, three samples were prepared and the assay was performed thrice to check the reproducibility (n = 3, N = 3). One-way ANOVA was performed for statistical measurements with $p < 0.05$.

2.5. Cell adhesion/endocytosis experiment

10^4 HEK293 cells were seeded on coverslips and grown for 24 hours in DMEM complete medium at 37 °C in a 5% CO_2 humidified chamber. After 24 hours, cells were incubated with 150 μg ml^{-1} of $Sc_{0.98}Er_{0.02}AlO_3$ perovskite compound for 24 hours, then washed thrice with 1× PBS, fixed with 4% PFA for 30 minutes and washed thrice with 1× PBS. Coverslips containing the cells were mounted on fresh slides using 70% glycerol for two-photon imaging.

2.6. Two-photon microscopy

An Olympus FVMPE-RS two-photon imaging system fitted with a 10× and a 40× UPlanSA objective lens was used to capture the images. The instrument was driven using an Insight X3 Spectra-Physics Ti:sapphire IR tunable laser (690–1300 nm). Full-field images were initially acquired at 40× magnification with constant gain settings and regions of interest across the samples. The excitation wavelength of the green channel was 764 nm. The laser intensity of the green channel was kept at 10%. Z-Scanning was performed during imaging to confirm the location of particles (1 mm *XY* slices were serially acquired). ImageJ software was used for background correction and further processing of the images.

3. Results and discussion

3.1. Structure and morphology

The room temperature powder X-ray diffraction patterns of high-pressure synthesized $Sc_{1-x}Er_xAlO_3$ (x = 0.01, 0.02, 0.03, 0.04) are depicted in Fig. 1(a). All the XRD patterns demonstrate excellent agreement with the reported one (ICSD#66883), indicating the phase purity of the compounds with an increase in Er^{3+} ion substitution in the host $ScAlO_3$. The inset shows a shift of the (112) peak to a lower angle, indicating the successful substitution of Er^{3+} ions. This can be understood by considering the size of the Sc^{3+} and Er^{3+} ions. The latter has a higher size (0.89 Å) than the former cation (0.745 Å), signifying lattice expansion upon Er^{3+} substitution. To get a better insight into the structure and further verify the phase purity, we have performed Rietveld refinement, as shown in Fig. 1(b) and Fig. S1 (ESI†). The crystal structure and the obtained refinement parameters for the $Sc_{0.98}Er_{0.02}AlO_3$ compound are shown in Fig. 1(c) and Table 1, respectively. The title compound crystallizes in an orthorhombic *Pbnm* space group (no. 62) and exhibits a 3D perovskite framework. The A-site of the compound is occupied by the Sc^{3+}/Er^{3+} ions surrounded by eight oxygen atoms, while AlO_6 octahedra are arranged in a corner-sharing fashion at the B-site. Notably, the electric dipole

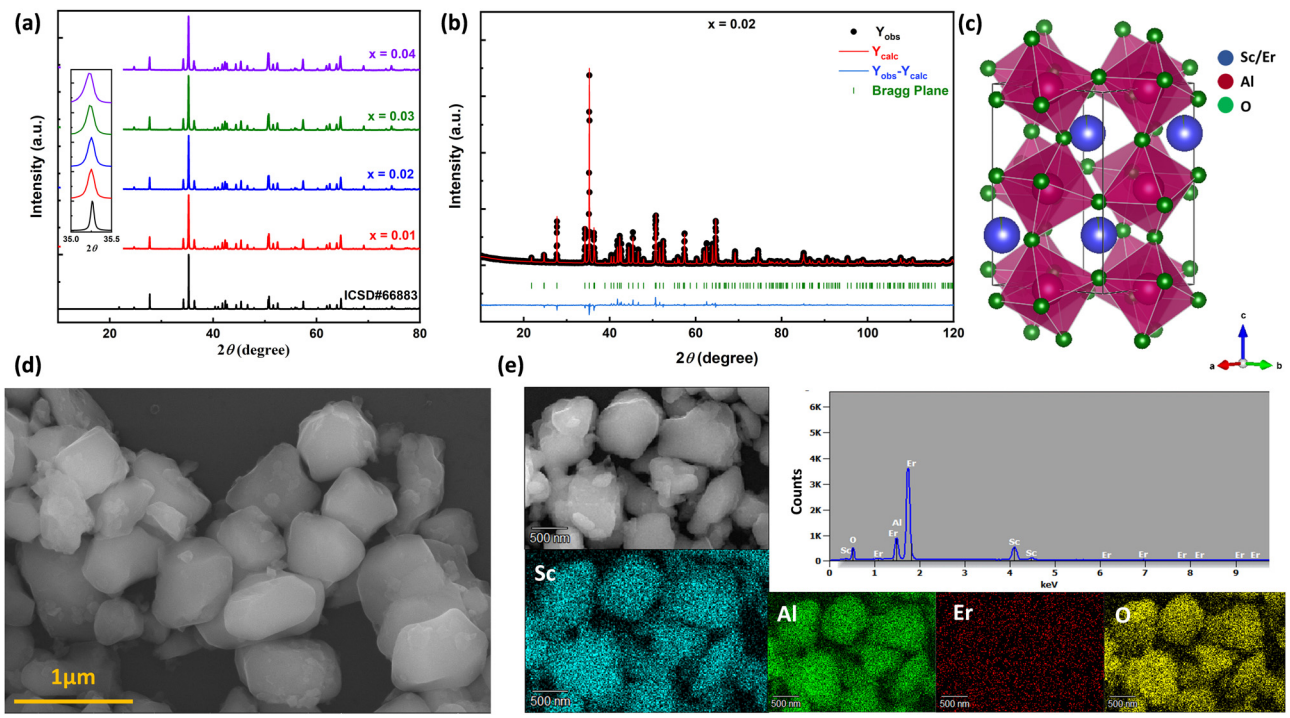

Fig. 1 (a) Room temperature powder X-ray diffraction patterns of $Sc_{1-x}Er_xAlO_3$ by varying x from 0.01 to 0.04. The inset shows the shift of the (112) peak towards a lower angle with increasing Er^{3+} ion concentration. (b) Rietveld refinement and (c) crystal structure of the $Sc_{0.98}Er_{0.02}AlO_3$ perovskite. (d) FESEM image showing microcrystals. (e) EDS spectra and elemental color mapping indicating successful Er substitution and its uniform distribution.

Table 1 Structural parameters of the $Sc_{0.98}Er_{0.02}AlO_3$ compound obtained from Rietveld refinement of powder XRD data

Atom	Wyckoff position	x	y	z	B_{iso}	Occupancy	Site symmetry
Sc	4*c*	0.9795(2)	0.0692(1)	1/4	0.302(25)	0.98	*m*
Er	4*c*	0.9795(2)	0.0692(1)	1/4	0.302(25)	0.02	*m*
Al	4*b*	0	$\frac{1}{2}$	0	0.269(39)	1.0	−1
O1	4*c*	0.1223(6)	0.4565(6)	1/4	1.0	1.0	*m*
O2	8*d*	0.6913(5)	0.3048(5)	0.0602(3)	1.0	1.0	1

Space group: *Pbnm*, a = 4.9415(1) Å, b = 5.2345(1) Å, c = 7.2051(1) Å, V = 186.374 Å^3, χ^2 = 3.42, R_p = 6.1%, R_{wp} = 8.03%.

moment induced intense emission in rare-earth activated compounds can be observed when the lanthanide ion occupies a local noncentrosymmetric site. In this compound, the Sc^{3+} cation occupies a polar site *m* at Wyckoff position 4*c*; hence, we have substituted the erbium ion at the A-site. The successful substitution of Er^{3+} in $ScAlO_3$ can be understood by comparing the lattice parameters and volume in $Sc_{1-x}Er_xAlO_3$. Since the ionic radius of Er^{3+} ions (0.89 Å) is higher than that of Sc^{3+} ions (0.745 Å), the lattice parameters and the volume of the unit cell should increase with Er^{3+} incorporation and the same can be observed in Fig. S2 (ESI†). In addition, we have performed FESEM and EDX measurements to further investigate the morphology and presence of Er^{3+} in the sample. Fig. 1(d) shows the FESEM image of the high-pressure synthesized $Sc_{0.98}Er_{0.02}AlO_3$ compound. The particles are agglomerated and exhibit irregular morphology. The grain size ranges from 300 to 800 nm, indicating their compatibility in the cell for potential bioimaging application. Besides, the elemental composition obtained from the EDS spectrum is consistent with the formula unit, as mentioned in Table S1 (ESI†). The elemental color mapping (Fig. 1(e)) indicates the uniform distribution of dopant ions in the sample. It is noteworthy that a rigid structure leads to a better phosphor host. The temperature-dependent heat capacity was fitted with the Debye equation, and the Debye temperature was calculated as[17]

$$\theta_D = \left(\frac{12\pi^4 N k_B}{5\beta}\right)^{\frac{1}{3}} \quad (1)$$

where *N* and k_B are the number of atoms in the formula unit multiplied by Avogadro's number and the Boltzmann constant, respectively. The obtained θ_D for this high-pressure synthesized compound is 672.2 K (Fig. S3, ESI†) which is much higher than those for some of the metal oxide hosts,[17] indicating that it is a better phosphor host.

3.2. UV-Vis diffuse reflectance spectroscopy

The optical bandgap of the high-pressure synthesized 2% Er^{3+}-doped $ScAlO_3$ compound is calculated from the UV-Vis absorption spectrum depicted in Fig. 2(a). First, the reflectance spectrum was collected and later converted to absorbance using the Kubelka–Munk equation:[42] $F(R) = (1-R)^2/2R = K/S$, where $F(R)$ represents the absorbance, *R* is the reflectance (%), and *K* and *S* represent the absorption and scattering coefficients, respectively. For a luminescent compound, it is important for the host lattice to be optically transparent in the visible region. This perovskite compound exhibits a bandgap of 3.35 eV and is feasible for Er-emission.

3.3. Photoluminescence properties

The Er^{3+}-activated $ScAlO_3$ compound displays green emission under UV light excitation. Fig. 2(b) shows the photoluminescence excitation (PLE) spectra of the $Sc_{0.98}Er_{0.02}AlO_3$ compound. The PLE spectrum recorded by monitoring the emission at λ_{em} = 546 nm demonstrates a number of sharp excitation peaks stemming from the f–f transition of Er^{3+} ions. The peaks at 357, 368, 382, 409, 451, and 493 nm correspond to the $^4I_{15/2} \rightarrow {}^2G_{7/2}$, $^4I_{15/2} \rightarrow {}^4G_{9/2}$, $^4I_{15/2} \rightarrow {}^4G_{11/2}$, $^4I_{15/2} \rightarrow {}^2H_{9/2}$, $^4I_{15/2} \rightarrow {}^4F_{5/2}$, and $^4I_{15/2} \rightarrow {}^4F_{7/2}$ transitions.[43] Although some of the transitions obey the spin selection rule ($\Delta S = 0$), all are parity forbidden (since, for all f–f transitions, $\Delta l = 0$).[44] Nonetheless, the admixing of opposite angular momentum orbitals can relax the parity selection rule and can be achieved when the lanthanide ion occupies a local noncentrosymmetric crystallographic site.[20] In the title compound, the Er^{3+} ion occupies the polar site symmetry *m* as discussed above, signifying the electric dipole moment induced transitions. Additionally, the sharp excitation at 382 nm indicates its potential for n-UV chip-based optoelectronic application.

Since the $^4I_{15/2} \rightarrow {}^4G_{11/2}$ transition is the most intense, the sample was excited at 382 nm and the respective emission spectrum is shown in Fig. 2(c). It illustrates a number of sharp emission peaks resulting from the excited f orbitals to the ground state transitions. The peaks at 524, 546, and 663 nm can be attributed to the $^2H_{11/2} \rightarrow {}^4I_{15/2}$, $^4S_{3/2} \rightarrow {}^4I_{15/2}$, and $^4F_{9/2} \rightarrow {}^4I_{15/2}$ transitions.[24] These sharp transitions are perceptive to the crystal environment, which allows the excitation involving even ΔJ. Further, the Commission International de l'Eclairage (CIE) chromaticity diagram for this phosphor is illustrated in Fig. S4 (ESI†). The chromaticity coordinates of (0.29, 0.70) ensure green emission and its potential for the green LED

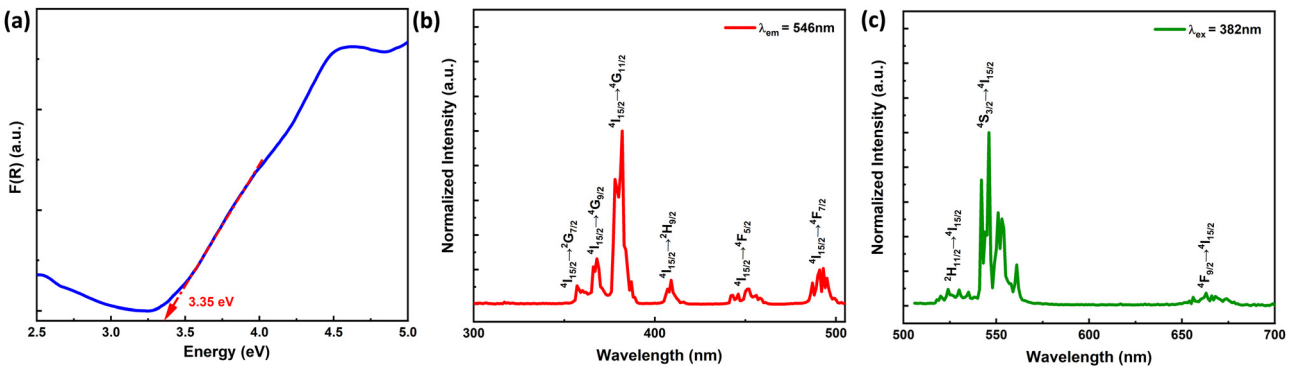

Fig. 2 (a) UV-Vis absorbance spectrum showing the band gap of the compound. (b) Photoluminescence excitation and (c) emission spectra of the $Sc_{0.98}Er_{0.02}AlO_3$ compound.

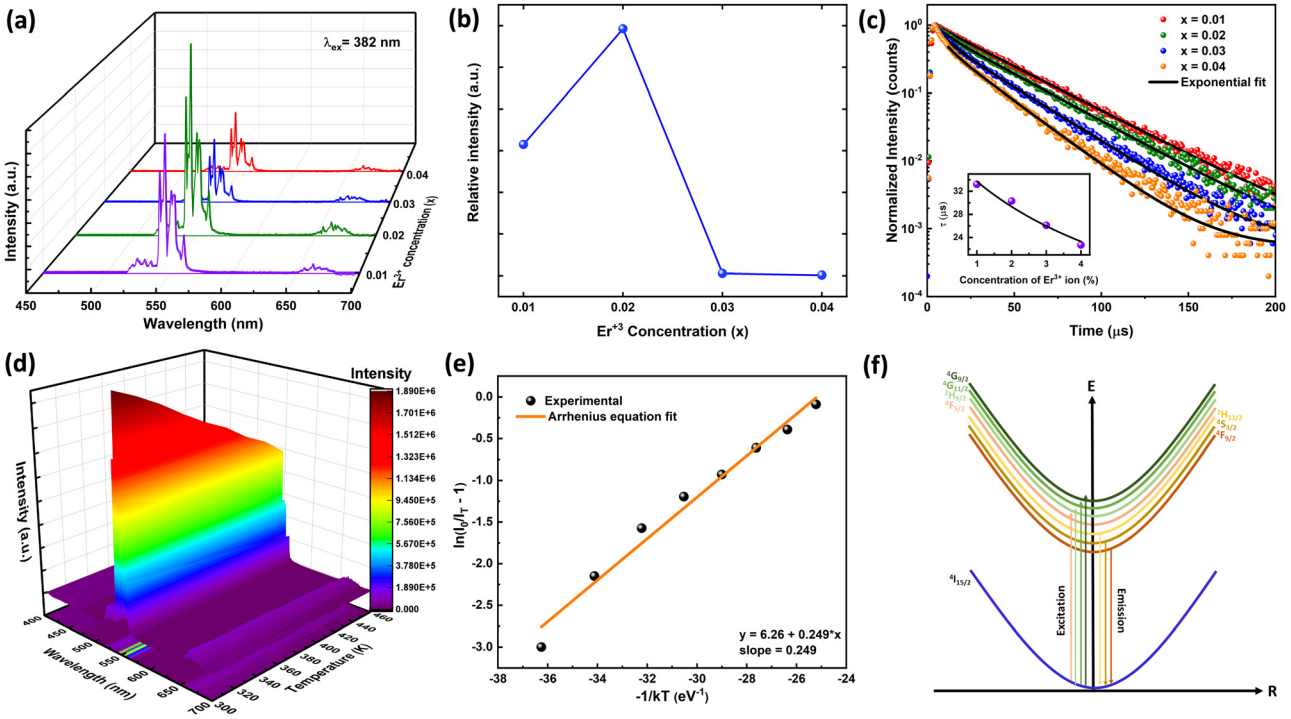

Fig. 3 (a) The PL spectra by varying Er^{3+} concentration in the $ScAlO_3$ lattice. (b) The variation of PL intensity with Er^{3+} showing concentration quenching at x = 0.02. (c) Time-resolved PL spectra of $Sc_{1-x}Er_xAlO_3$. The inset shows Auzel's model fitting to lifetime *vs.* activator concentration. (d) Pseudo-color temperature-dependent emission spectra. (e) Arrhenius model fitting exhibits a binding energy of 0.249 eV. (f) The schematic diagram of the electronic excitation process in Er^{3+} ions.

application. The PLQY is 3.2% for the $Sc_{0.98}Er_{0.02}AlO_3$ compound.

The PLE and PL spectra by varying the concentration of Er^{3+} ions in the $ScAlO_3$ matrix are shown in Fig. S5 (ESI†) and Fig. 3(a), respectively. The peak shape of excitation and emission spectra did not change when altering the dopant concentration. However, the relative emission intensity changed. Initially, with an increase in the Er^{3+}-substitution, the emission intensity was enhanced owing to the increase in luminescent centers. At x = 0.02, the emission was maximum, and with further increase in the rare-earth ion concentration, the intensity declines (Fig. 3(b)). The decrease in intensity can be attributed to the concentration quenching phenomenon.[45] With increasing the dopant concentration, the distance between two rare-earth ions decreases, resulting in effective energy transfer among themselves. The energy transfer process is mainly governed by the critical distance (R_c), which can be determined as[45]

$$R_c = 2\left(\frac{3V}{4\pi x_c N}\right)^{\frac{1}{3}} \quad (2)$$

Here V represents the unit cell volume, and x_c and N are the critical concentration and the number of emitting lattice sites in the unit cell, respectively. In the present case, x_c and N are 0.02 and 1, respectively. V was obtained to be 186.374 Å^3 from the Rietveld refinement of the XRD pattern of $Sc_{0.98}Er_{0.02}AlO_3$. The critical distance of 25.45 Å speculates a multipole–multipole type interaction among Er^{3+} ions rather than exchange interaction.

3.4. Time-resolved photoluminescence

The time-resolved photoluminescence spectra of $Sc_{1-x}Er_xAlO_3$ ($0.01 \leq x \leq 0.04$) were recorded by exciting the samples at 382 nm by monitoring the PL at 546 nm and are illustrated in Fig. 3(c). The PL lifetimes were obtained by fitting the decay curves with a single exponential model:[40,46]

$$I_t = I_0 + Ae^{-\frac{t}{\tau}} \quad (3)$$

Here I_t and I_0 indicate the emission intensities at time t and 0, respectively. A is a constant and t represents the PL lifetime of the compounds mentioned in Table 2. The monoexponential behaviour manifests a single emitting channel consistent with the Er^{3+} site occupancy. The rare-earth ion occupies a single crystallographic site, ultimately generating a single emitting channel. In addition, the PL lifetime decreases from 33.2 to 22.7 μs with a rise in dopant concentration. This can be attributed to the decrease in Er^{3+}–Er^{3+} distance enhancing the interaction, resulting in a faster decay process. However, at a higher Er^{3+} concentration, the decaying nature has slightly

Table 2 The photoluminescence lifetime and theoretical internal quantum efficiency (IQE) of $Sc_{1-x}Er_xAlO_3$ ($0.01 \leq x \leq 0.04$) perovskites

x	τ (μs)	IQE (%)
0.01	33.2	83.8
0.02	30.3	76.5
0.03	26.1	65.9
0.04	22.7	57.3

deviated from the single exponential nature because of the energy transfer process among the activator ions leading to an additional decay channel.[40] The inset of Fig. 3(c) demonstrates the relationship between the PL lifetime and Er^{3+} concentration fitted with Auzel's model:[47]

$$\tau(c) = \frac{\tau_0}{1 + \frac{c}{c_0}\exp\left(-\frac{N}{3}\right)} \quad (4)$$

where $\tau(c)$ is the obtained PL lifetime from TRPL measurement at concentration c, τ_0 represents the internal radiative lifetime, and N represents the number of phonons required for PL quenching. To estimate the value of N, we have performed Raman spectroscopy measurement of $Sc_{0.98}Er_{0.02}AlO_3$ and the spectrum is shown in Fig. S6 (ESI†). Since the maximum energy phonon mode is at around 1000 cm^{-1}, ~18 phonons (N) are required to quench the PL at 546 nm or 18 315 cm^{-1}. Hence, the obtained intrinsic lifetime (τ_0) is 39.6 μs which can be useful to calculate the theoretical internal quantum efficiency (IQE) η using the relation $\eta = \tau(c)/\tau_0$.[48] The calculated η values for $Sc_{1-x}Er_xAlO_3$ phosphors are listed in Table 2.

3.5. Temperature-dependent photoluminescence

We have performed the temperature-dependent PL measurement of $Sc_{0.98}Er_{0.02}AlO_3$ to investigate the PL stability and activation energy. Fig. 3(d) represents the pseudo-color plot of temperature-dependent emission spectra. Although the line width and peak shape did not change with increasing temperature, the intensity deteriorated. This is the thermal quenching effect and can be understood using the Arrhenius model:[49]

$$\ln\left(\frac{I_0}{I_T} - 1\right) = \ln\ A - \frac{E_a}{kT} \quad (5)$$

Here I_0 and I_T are the emission intensities measured at 300 K and temperature T. A is the ratio of the nonradiative rate to the radiative rate and termed as the quenching frequency factor. E_a and k represent the activation energy or binding energy of the exciton and the Boltzmann constant, respectively. To obtain the binding energy, we have performed the linear fitting to the $\ln(I_0/I_T - 1)$ *vs.* $-1/kT$ plot as shown in Fig. 3(e). An activation energy of 0.249 eV is required to dissociate the exciton in the title compound. To determine PL thermal stability, we have calculated $TQ_{1/2}$, which is the temperature at which the emission efficiency decreases to half of its initial value, using the formula:[50]

$$TQ_{1/2} = \frac{-E_a}{k \times \ln\left(\frac{1}{A}\right)} \quad (6)$$

The obtained $TQ_{1/2}$ of 462 K exhibits excellent thermal stability and its potential for optoelectronic application. Fig. 3(f) illustrates a schematic diagram of electronic transition in the PL excitation and emission process. Under 382 nm excitation, the $^4G_{11/2}$ state can be populated. By multiphonon emission or internal crossing, the excited electrons decay to the lower energy states $^2H_{11/2}$, $^4S_{3/2}$, and $^4F_{9/2}$. The electrons from these aforementioned states can return to the ground state $^4I_{15/2}$ radiatively, giving rise to a sharp emission line. There might be an energy difference of 0.249 eV between the bottom of the $^4S_{3/2}$ and its crossover point with the $^4I_{15/2}$ state, responsible for the thermal quenching effect.

3.6. Biocompatibility and *in vitro* bioimaging

Since the $Sc_{0.98}Er_{0.02}AlO_3$ perovskite compound exhibits the highest luminescence intensity, we have used it for *in vitro* bioimaging application. First, we checked the PL properties of this compound using two-photon microscopy upon dispersing it in Milli-Q water. We observed strong green luminescence of the $Sc_{0.98}Er_{0.02}AlO_3$ perovskite compound when excited at 764 nm (Fig. S7, ESI†). Therefore, we speculated that this compound could be used as a bio-imaging tool. A compound can be used as a bio-imaging marker only if it does not have adverse effects on the cells. Hence, we investigated the cytotoxicity of this compound using a standard MTT assay first in HEK293 cells, followed by SH-SY5Y neuroblastoma cells. HEK293 cells were treated with various concentrations ranging from 10 μg ml^{-1} to 400 μg ml^{-1} of the $Sc_{0.98}Er_{0.02}AlO_3$ compound for 24 hours. The cell viability of HEK293 cells was maintained at >90% and did not vary significantly until 250 μg ml^{-1} concentration (Fig. 4(a)). Moreover, we observed significantly increased toxicity with increasing concentration above 250 μg ml^{-1}, but the cell viability was still greater than 65% until 400 μg ml^{-1} of compound concentration. The above results imply that this compound has extremely low cytotoxicity and good biocompatibility until 250 μg ml^{-1} concentration in HEK293 cells. Additionally, we also investigated the cytotoxicity in completely different and complex SH-SY5Y neuroblastoma cells. Interestingly, the cell viability of SH-SY5Y cells was found to be >80% up to 250 μg ml^{-1} concentration with insignificant cell toxicity, as shown in Fig. 4(b). These results demonstrate that the $Sc_{0.98}Er_{0.02}AlO_3$ compound has low cytotoxicity and good biocompatibility, thus implying its potential for *in vitro* and *in vivo* bioimaging applications.

To investigate the potential of this compound for *in vivo* bioimaging, we next analyzed the uptake/entry of these particles after 24 hours of treatment in HEK293 cells at 200 μg ml^{-1} concentration. Two-photon microscopy imaging was performed by exciting the sample at 764 nm. We observed a green luminescence signal inside the cells, which shows that the particles of the

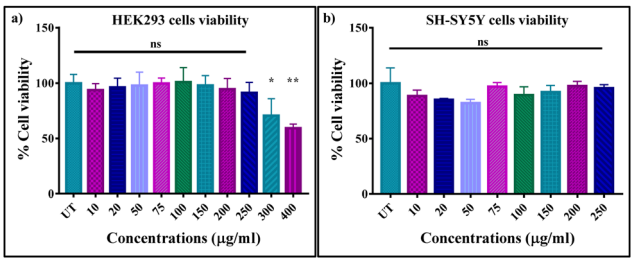

Fig. 4 *In vitro* cell viability of (a) HEK293 and (b) SH-SY5Y cells incubated with different concentrations of the $Sc_{0.98}Er_{0.02}AlO_3$ perovskite compound for 24 h. The standard error of mean is shown as error bars.

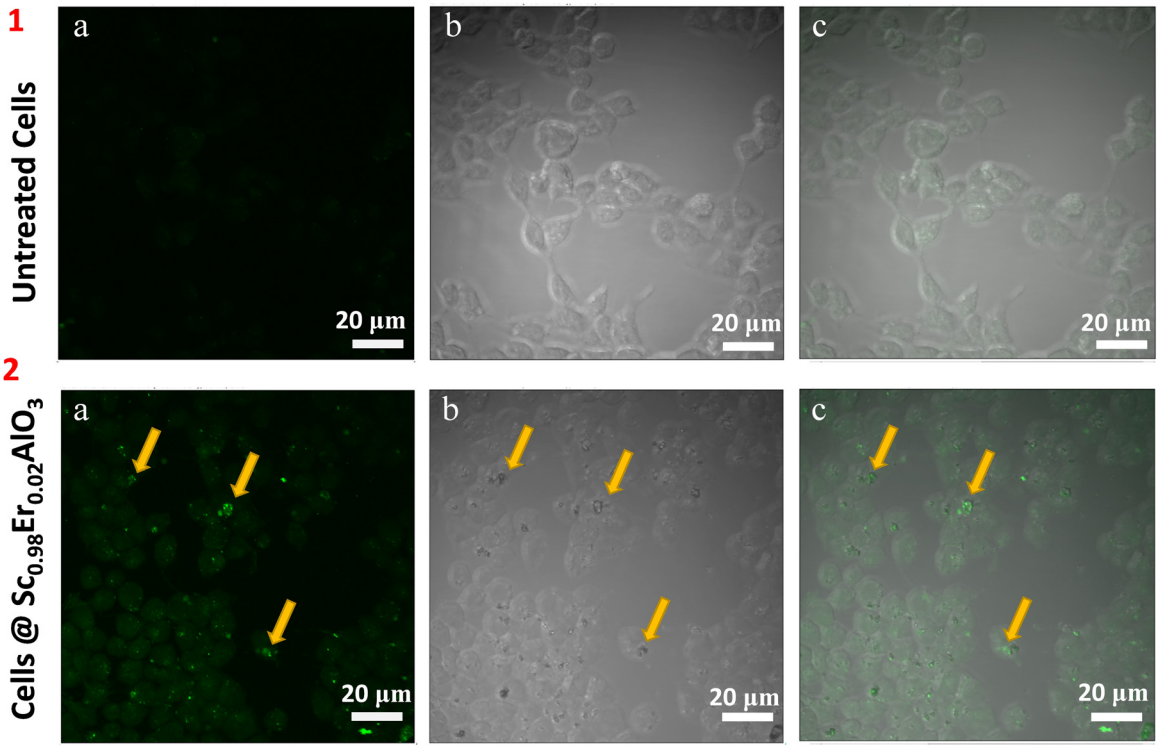

Fig. 5 Localization of oxide particles in HEK293 cells. Two-photon microscopy image of untreated HEK293 cells (panel 1) and $Sc_{0.98}Er_{0.02}AlO_3$ perovskite treated cells (panel 2). Images were split into their individual channels: green (1a and 2a), bright field (1b and 2b), and merge (1c and 2c). Yellow arrows mark the oxide particles present inside the HEK293 cells. Identical settings and gains were used across all the samples during the imaging. Scale bar: 20 μm.

title compound have entered and are present within the HEK293 cells (Fig. 5, panel 2). Untreated cells were used as control, where green luminescence was absent, as depicted in Fig. 5 (panel 1). Since the green luminescence results after the treatment of perovskite particles, it confirms the absence of an artifact. Also, the z-scan images shown in Fig. S8 (ESI†) suggest that the treated particles have diffused inside the cells. Interestingly we did not observe photobleaching or blinking of these particles after treatment in the cell line. These results imply the potential application of this compound for *in vivo* bioimaging.

4. Conclusions

$Sc_{1-x}Er_xAlO_3$ ($0.01 \leq x \leq 0.04$) compounds were prepared using the high-pressure synthesis technique. These compounds crystallize in an orthorhombic *Pbnm* space group with a perovskite structure, where Er^{3+} ions occupy a polar site symmetry *m*. These compounds exhibit green emission upon UV light excitation. The critical distance for concentration quenching is around 25.45 Å, which speculates a multipole–multipole type interaction among the activator ions. The binding energy and $TQ_{1/2}$ of 0.249 and 462 K indicate the excellent thermal photostability of the compound. Besides, the PL lifetime lies in the order of microseconds. Due to the sharp emission line, long luminescence lifetime, and absence of photoblinking or photobleaching, we have checked the cytotoxicity of this compound, which demonstrates excellent cell viability in HEK293 and SH-SY5Y cells. The analysis of two-photon microscopy images confirms the successful diffusion of the title compound in the HEK293 cells, which indicates its potential biomedical applications. Moreover, several diseases like muscular dystrophy and neurological disorder pathophysiology can be tracked using this system.

Conflicts of interest

There are no conflicts to declare.

Acknowledgements

The authors thank the International Centre for Materials Science (ICMS) and Sheik Saqr Laboratory (SSL) of Jawaharlal Nehru Centre for Advanced Scientific Research (JNCASR) for the experimental facility. D. P. P. thanks the Council of Scientific and Industrial Research (CSIR) for the research fellowship. AKS acknowledges JNCASR for financial support. TKK acknowledges the J C Bose Fellowship from SERB (DST), Government of India.

Notes and references

1 T. He, K. A. Regan, N. Rogado, M. A. Hayward, M. K. Haas, J. S. Slusky, K. Inumara, H. W. Zandbergen and R. J. Cava, *Nature*, 2001, **411**, 54–56.

2 P. Mandal, V. S. Bhadram, Y. Sundarayya, C. Narayana, A. Sundaresan and C. N. R. Rao, *Phys. Rev. Lett.*, 2011, **107**, 137202.
3 A. T. Mulder, N. A. Benedek, J. M. Rondinelli and C. J. Fennie, *Adv. Funct. Mater.*, 2013, **23**, 4810–4820.
4 C. M. Fernández-Posada, A. Castro, J. M. Kiat, F. Porcher, O. Peña, M. Algueró and H. Amorín, *Nat. Commun.*, 2016, **7**, 1–9.
5 J. Hwang, R. R. Rao, L. Giordano, Y. Katayama, Y. Yu and Y. Shao-Horn, *Science*, 2017, **358**, 751–756.
6 T. Ye, X. Wang, X. Li, A. Q. Yan, S. Ramakrishna and J. Xu, *J. Mater. Chem. C*, 2017, **5**, 1255–1260.
7 H. Hu, S. A. Morris, X. Qiao, D. Zhao, T. Salim, B. Chen, E. E. M. Chia and Y. M. Lam, *J. Mater. Chem. C*, 2018, **6**, 10301–10307.
8 R. Chiara, M. Morana, G. Folpini, A. Olivati, B. Albini, P. Galinetto, L. Chelazzi, S. Ciattini, E. Fantechi, S. A. Serapian, A. Petrozza and L. Malavasi, *J. Mater. Chem. C*, 2022, 12367–12376.
9 C. Li, Z. Zang, C. Han, Z. Hu, X. Tang, J. Du, Y. Leng and K. Sun, *Nano Energy*, 2017, **40**, 195–202.
10 H. Guan, S. Zhao, H. Wang, D. Yan, M. Wang and Z. Zang, *Nano Energy*, 2020, **67**, 104279.
11 D. Yan, T. Shi, Z. Zang, T. Zhou, Z. Liu, Z. Zhang, J. Du, Y. Leng and X. Tang, *Small*, 2019, **15**, 1901173.
12 D. Yan, S. Zhao, Y. Zhang, H. Wang and Z. Zang, *Opto-Electron. Adv.*, 2022, **5**, 200071.
13 E. Montanari, L. Righi, G. Calestani, A. Migliori, E. Gilioli and F. Bolzoni, *Chem. Mater.*, 2005, **17**, 1765–1773.
14 P. N. Shanbhag, T. Thao Tran, P. Shiv Halasyamani, A. Sundaresan and C. N. R. Rao, *J. Solid State Chem.*, 2018, **265**, 79–84.
15 G. Blasse and B. C. Grabmaier, *Luminescent materials*, Springer, 1994, pp. 1–9.
16 M. Shang, S. Huang, P. Dang, J. Lin, Y. Yan and M. Deng, *J. Mater. Chem. C*, 2022, **10**, 14971–14981.
17 K. A. Denault, J. Brgoch, S. D. Kloß, M. W. Gaultois, J. Siewenie, K. Page and R. Seshadri, *ACS Appl. Mater. Interfaces*, 2015, **7**, 7264–7272.
18 A. A. Haider, Y. Cun, X. Bai, Z. Xu, Y. Zi, J. Qiu, Z. Song, A. Huang and Z. Yang, *J. Mater. Chem. C*, 2022, **10**, 6243–6251.
19 X. Li, B. Milićević, M. D. Dramićanin, X. Jing, Q. Tang, J. Shi and M. Wu, *J. Mater. Chem. C*, 2019, **7**, 2596–2603.
20 A. R. Sharits, J. F. Khoury and P. M. Woodward, *Inorg. Chem.*, 2016, **55**, 12383–12390.
21 X. Liu, Z. Xu, C. Chen, D. Tian, L. Yang, X. Luo, A. A. Al Kheraif and J. Lin, *J. Mater. Chem. C*, 2019, **7**, 2361–2375.
22 M. Guzik, E. Tomaszewicz, Y. Guyot, J. Legendziewicz and G. Boulon, *J. Mater. Chem. C*, 2015, **3**, 8582–8594.
23 M. Pokhrel, G. A. Kumar, C. G. Ma, M. G. Brik, B. W. Langloss, I. N. Stanton, M. J. Therien, D. K. Sardar and Y. Mao, *J. Mater. Chem. C*, 2015, **3**, 11486–11496.
24 W. Ran, H. M. Noh, S. H. Park, B. R. Lee, J. H. Kim, J. H. Jeong and J. Shi, *Dalton Trans.*, 2019, **48**, 4405–4412.
25 M. Wu, E. H. Song, Z. T. Chen, S. Ding, S. Ye, J. J. Zhou, S. Q. Xu and Q. Y. Zhang, *J. Mater. Chem. C*, 2016, **4**, 1675–1684.
26 R. Wei, F. Lu, L. Wang, F. Hu, X. Tian and H. Guo, *J. Mater. Chem. C*, 2022, **10**, 9492–9498.
27 Y. Zhang, D. Geng, X. Li, J. Fan, K. Li, H. Lian, M. Shang and J. Lin, *J. Phys. Chem. C*, 2014, **118**, 17983–17991.
28 M. M. A. Abualrejal, K. Eid, R. Tian, L. Liu, H. Chen, A. M. Abdullah and Z. Wang, *Chem. Sci.*, 2019, **10**, 7591–7599.
29 W. Li, D. Wang, X. Li, P. Li, P. Fu, C. Hu, J. Hao, W. Li and Q. Zhang, *J. Mater. Chem. C*, 2022, 11891–11902.
30 H. Xu, Y. Lian, Z. Lu, I. Kolesnikov, Y. Zhao, K. He, Z. Su, G. Bai and S. Xu, *J. Mater. Chem. C*, 2022, **10**, 10660–10668.
31 E. MacÉ, G. Montaldo, I. Cohen, M. Baulac, M. Fink and M. Tanter, *Nat. Methods*, 2011, **8**, 662–664.
32 P. Lei, P. Zhang, Q. Yuan, Z. Wang, L. Dong, S. Song, X. Xu, X. Liu, J. Feng and H. Zhang, *ACS Appl. Mater. Interfaces*, 2015, **7**, 26346–26354.
33 T. Shen, Y. Zhang, A. M. Kirillov, H. Cai, K. Huang, W. Liu and Y. Tang, *Chem. Commun.*, 2016, **52**, 1447–1450.
34 G. Gou, T. Fan, M. Wang and L. Li, *J. Mater. Chem. C*, 2022, 12402–12412.
35 M. Nyk, R. Kumar, T. Y. Ohulchanskyy, E. J. Bergey and P. N. Prasad, *Nano Lett.*, 2008, **8**, 3834–3838.
36 X. Wu, H. Liu, J. Liu, K. N. Haley, J. A. Treadway, J. P. Larson, N. Ge, F. Peale and M. P. Bruchez, *Nat. Biotechnol.*, 2003, **21**, 41–46.
37 X. Michalet, F. F. Pinaud, L. A. Bentolila, J. M. Tsay, S. Doose, J. J. Li, G. Sundaresan, A. M. Wu, S. S. Gambhir and S. Weiss, *Science*, 2005, **307**, 538–544.
38 J. Shen, L.-D. Sun and C.-H. Yan, *Dalton Trans.*, 2008, 5687–5697.
39 C. Bouzigues, T. Gacoin and A. Alexandrou, *ACS Nano*, 2011, **5**, 8488–8505.
40 D. P. Panda, A. K. Singh, T. K. Kundu and A. Sundaresan, *J. Mater. Chem. B*, 2022, **10**, 935–944.
41 T. A. Pomelova, V. V. Bakovets, I. V. Korol'kov, O. V. Antonova and I. P. Dolgovesova, *Phys. Solid State*, 2014, **56**, 2496–2506.
42 P. Kubelka and F. Munk, *Z. Tech. Phys.*, 1931, **12**, 259–274.
43 Y. Liu, Y. Liu, G. Liu, X. Dong and J. Wang, *RSC Adv.*, 2015, **5**, 97995–98003.
44 S. V. Eliseeva and J.-C. G. Bünzli, *Chem. Soc. Rev.*, 2010, **39**, 189–227.
45 J. Zhou and Z. Xia, *J. Mater. Chem. C*, 2014, **2**, 6978–6984.
46 D. P. Panda, D. Swain, M. Chaudhary, S. Mishra, G. Bhutani, A. K. De, U. V. Waghmare and A. Sundaresan, *Inorg. Chem*, 2022, **61**, 17026–17036.
47 L. Bai, Q. Meng, X. Wang, M. Huo and Y. Sui, *Mater. Res. Bull.*, 2019, **111**, 306–310.
48 M. H. V. Werts, R. T. F. Jukes and J. W. Verhoeven, *Phys. Chem. Chem. Phys.*, 2002, **4**, 1542–1548.
49 D. P. Panda, D. Swain and A. Sundaresan, *J. Phys. Chem. C*, 2022, **126**, 13291–13299.
50 D. P. Panda, D. Swain and A. Sundaresan, *Inorg. Chem.*, 2022, **61**, 11377–11386.

